An Empirical Loss Model for an Additively Manufactured Luneburg Lens Antenna

Brian F. LaRocca[1] **and Mark S. Mirotznik**[2]

[1]Department of the Army
Aberdeen Proving Ground, Aberdeen, MD 21005, USA
brian.f.larocca.civ@army.mil

[2]Electrical Engineering Department
University of Delaware, Newark, DE 19716, USA
mirotzni@udel.edu

Abstract **–** This research applies Effective Medium Theory and 3D Finite Element Analysis to model the transmissive loss through a waveguide fed additively manufactured Luneburg lens. New results are presented that provide rational function approximations for accurately modeling the aperture, beam, and radiation loss factors of the antenna. It introduces a normalized loss tangent and shows that the loss factors are dependent on the product of this parameter and the lens radius. Applying the constraint that the main beam of the radiation pattern contains 50% of accepted power, a maximum useful radius is tabulated for common polymers used in additive manufacturing.

Index Terms **–** Additive manufacturing, dielectric loss, effective medium theory, lens antenna, luneburg lens.

I. INTRODUCTION

While spatially graded dielectrics, also known as graded-index (GRIN) structures, are popular devices in optics and photonics they have historically been used less frequently at radio frequencies (RF). However, there has been a surge of interest in using RF GRIN antennas as low-cost passive beam-formers. One of the most popular RF GRIN structures is the well-known Luneburg lens (LL) [1-6]. The LL is a spherical device in which every point on the surface is the focal point of a plane wave incident from the opposing surface. This unique property can be leveraged to realize passive beam steering antennas capable of directing a single or multiple beams over wide scan angles.

While the LL concept has been known for nearly 80 years [1], our ability to reliably manufacture them has been aided by recent advancements in additive manufacturing (AM) technologies and materials. Prior to AM, fabricating a structure with spatially graded dielectric properties was an expensive and challenging manufacturing problem.

Over the last eight years, a host of papers have been published on the use of AM to fabricate the LL and other GRIN devices [7-14]. While these previous studies have demonstrated AM's ability to fabricate functional RF GRIN lenses, what has not been well characterized is how the choice of AM material and unit cell architecture influences performance in terms of aperture, beam, and radiation efficiency. All which factor into the maximum useful gain that can be achieved for a particular design.

In this paper, a full wave computational study is presented that quantifies the effect of material choice and unit cell architecture on the performance of AM fabricated LL antennas. Specifically, the aperture, beam and radiation loss factors are evaluated as a function of the LL's material properties, unit cell geometry and overall electrical size. An empirical model is provided that accurately describes these relationships. This model is then used to predict the maximum useful gain of an antenna for a given material and unit cell structure. These results will serve as a useful guide for antenna design engineers when determining the specific AM fabrication materials and approach best suited for their application.

The product of lens radius in terms of free space wavelengths and the normalized loss tangent is introduced as being a key metric in characterizing the radiation pattern of a LL with loss. Although somewhat dependent upon the unit cell geometry, this product identifies three important thresholds. Listed in order of increasing severity they are as follows: (a) at a value of ≈ 0.06, the main lobe contains only 50% of the accepted power; (b) at a value of ≈ 0.3, the gain has reached the peak value that is possible for the given material and unit cell geometry. Increasing the lens size further results in a decrease in antenna gain; (c) at a value of ≈ 0.8, radiated

Submitted On: April 11, 2022
Accepted On: June 19, 2022

https://doi.org/10.13052/2022.ACES.J.370505

power is reduced to $\approx 13\%$ of the accepted power, and the main beam is nearly extinguished containing only $\approx 3\%$ of the radiated power.

The outline for the subsequent portion of the paper is as follows. Following an introduction to the computer model and workflow, Section II-A presents the effective medium models that represent unit cell structures. Section II-B provides the range of model parameters simulated. Section II-C defines the far-field loss factors for which rational functional approximations are given in Section II-D. The accuracy of these approximations is shown in Section III-A. The normalized loss tangent is introduced in Section III-B and applied to tabulate the maximum useful radius of common polymers used in the manufacture of GRIN components. Section III-C tabulates thresholds of performance in terms of the lens radius and normalized loss tangent product. Section IV further discusses the primary results and suggests future research.

II. MODELING AND ANALYSIS

The data for this research is derived using a computer model comprised of a spherical LL, an open-ended cylindrical waveguide, and a spherical Perfectly Matched Layer (PML). The lens model is inhomogeneous, continuous, and isotropic. Material loss is accounted for by incorporating Effective Medium Theory (EMT) to predict an effective loss tangent for the inhomogeneous air/material mixture that makes up the lens. The open-ended waveguide serves as the antenna feed, which supplies monochromatic and fundamental mode excitation. The PML allows for efficient simulation by providing a high-performance absorbing boundary that fully encloses the lens and waveguide. It effectively truncates the computational domain, such that the near field only be computed out to a short distance beyond the lens and waveguide.

Finite Element Analysis (FEA) of the above-described model is carried out using COMSOL Multiphysics software equipped with the RF Module [23]. Due to the complete symmetry of the model about the z axis, an otherwise 3D simulation is reduced to a 2D axisymmetric simulation. This results in enormous savings in computer resources, allowing for simulations that would not otherwise be possible on less than exotic computing platforms. A sketch of the axisymmetric model is provided in Fig. 1. The half-plane model is rotated 360° around the z axis to create a 3D model including a spherical lens, a cylindrical open ended waveguide port, and the spherical PML shell.

Upon completion of FEA for each parameter combination modeled, the COMSOL RF Module is used to convert the resulting electromagnetic field along the inner surface of the PML shell to the far-field gain. A 2D cut of the gain is saved to a text file with a unique name that identifies the parameter combination. Post-processing and visualization are carried out in MATLAB. Beyond extraction of boresight gain, this stage includes calculation of aperture efficiency η_a, radiation efficiency η_r, and beam efficiency η_b. The loss factor for each efficiency is computed, being a positive number defined in decibels as:

$$L_x = -10 \cdot \log_{10}(\eta_x). \tag{1}$$

Finally, the MATLAB Global Optimization Toolbox [24] is then used to provide a rational function approximation for each of the three loss factors, including a fourth, being $L_b + L_r$.

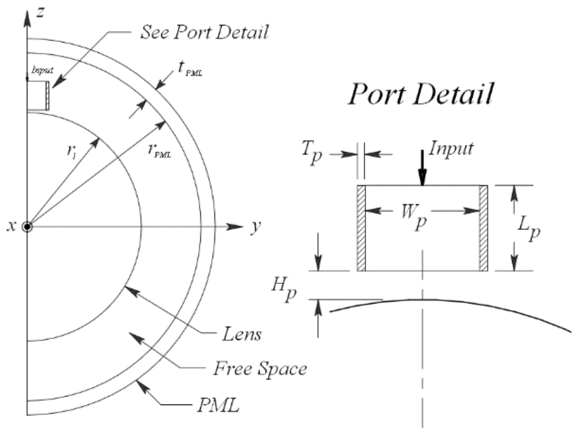

Fig. 1. 2D sketch of axisymmetric model used in the simulation.

A. Effective medium modeling

EMT provides a quantitative means to describe the properties of a composite material, knowing the ratio and properties of its individual constituents. In the case of an additively manufactured component such as the LL, the constituents are air and the printed material. Moreover, we are only interested in the effective permittivity of the resulting composite. Throughout the following, all permittivities are relative, and caret accents are used to denote a complex quantity.

The point of view adapted here is that the lens is a composite formed from a spherical host volume of free space, into which precise amounts of printed material are deposited. The material deposited thus forms discrete solid inclusions, having a natural complex relative permittivity $\hat{\varepsilon}$. In any region of the sphere, the effective permittivity of the composite in that region depends on the volumetric ratio of printed material to free space. This ratio is referred to as the volume fraction f and varies throughout the lens. Furthermore, it is necessary that the dimension of the largest inclusion be much smaller than the shortest operational wavelength required.

Starting with the definition for $\hat{\varepsilon}$:

$$\begin{aligned}\hat{\varepsilon} &= \varepsilon' - j\cdot\varepsilon'',\\ &= \varepsilon'\cdot\left(1 - j\cdot\frac{\varepsilon''}{\varepsilon'}\right),\\ &= \varepsilon'\cdot\left(1 - j\cdot\tan\left(\delta\right)\right).\end{aligned} \tag{2}$$

In (2), ε', ε'' and $tan(\delta)$ represent the dielectric constant, the imaginary component of $\hat{\varepsilon}$, and the loss tangent respectively of the printed material at the operational frequency.

EMT provides several quantitative relationships relating f, $\hat{\varepsilon}$ and the effective permittivity of the composite. These are termed mixing formulas, and this work employs the Maxwell Garnett (MG) and the Linear mixing formulas. It is shown below that the Linear mixing rule predicts a higher loss tangent for the composite than does the MG mixing rule. By providing results for both mixing rules, the intent is to provide a realistic range of values that may occur.

Allowing $\hat{\varepsilon}_{MG}$ to represent the MG prediction for the effective permittivity of the composite, and f_{MG} the respective volume fraction, we have [21]:

$$\begin{aligned}\hat{\varepsilon}_{MG} &= 1 + \frac{3f_{MG}\cdot(\hat{\varepsilon}-1)}{\hat{\varepsilon}+2-f_{MG}\cdot(\hat{\varepsilon}-1)},\\ &= \varepsilon'_{MG}\cdot\left(1 - j\cdot\tan\left(\delta_{MG}\right)\right).\end{aligned} \tag{3}$$

For materials where $\varepsilon'' \ll \varepsilon'$, the following observation is useful [21]:

$$\varepsilon'_{MG} \approx 1 + \frac{3f_{MG}\cdot(\varepsilon'-1)}{\varepsilon'+2-f_{MG}\cdot(\varepsilon'-1)}. \tag{4}$$

Now, in terms of the cylindrical coordinate system (r_c, z, ϕ) used for the 2D axisymmetric model [23], the Luneburg permittivity distribution ε_{LB} is given by:

$$\varepsilon_{LB} = 2 - \left(\frac{r_c^2+z^2}{r_l^2}\right), \tag{5}$$

where r_l denotes the radius of the LL measured in free-space wavelengths λ. This is a real quantity, and it is necessary that the volume fraction throughout the lens, be set such that the real component of the effective permittivity results in ε_{LB}. Thus, setting $\varepsilon'_{MG} = \varepsilon_{LB}$, and solving for f_{MG} in (4), we have:

$$f_{MG} \approx \frac{2\varepsilon_{LB}-\varepsilon'+\varepsilon'\varepsilon_{LB}-2}{2\varepsilon'-\varepsilon_{LB}+\varepsilon'\varepsilon_{LB}-2}. \tag{6}$$

A similar procedure is carried out in determining the volume fraction for modeling Linear mixing; however, the relationship is now exact. Allowing $\hat{\varepsilon}_{Lin}$ to represent the Linear mixture prediction for the effective permittivity of the composite, and f_{Lin} the respective volume fraction, we have [21]:

$$\begin{aligned}\hat{\varepsilon}_{Lin} &= (1-f_{Lin}) + f_{Lin}\cdot\hat{\varepsilon},\\ &= \varepsilon'_{Lin}\cdot\left(1 - j\cdot\tan\left(\delta_{Lin}\right)\right).\end{aligned} \tag{7}$$

The real component of (7) is:

$$\varepsilon'_{Lin} = 1 + f_{Lin}\cdot\left(\varepsilon'-1\right), \tag{8}$$

and, upon setting $\varepsilon'_{Lin} = \varepsilon_{LB}$, and solving for f_{Lin} in (8), we have:

$$f_{Lin} = \frac{\varepsilon_{LB}-1}{\varepsilon'-1}. \tag{9}$$

As an illustrative example, ε'_{Lin} and $\tan(\delta_{Lin})$ are shown in Fig. 2 across a planar slice through the center of a LL. The material used has a dielectric constant of 4.0 and a loss tangent of 0.1, i.e., $\hat{\varepsilon} = 4\cdot(1-j\cdot 0.1)$.

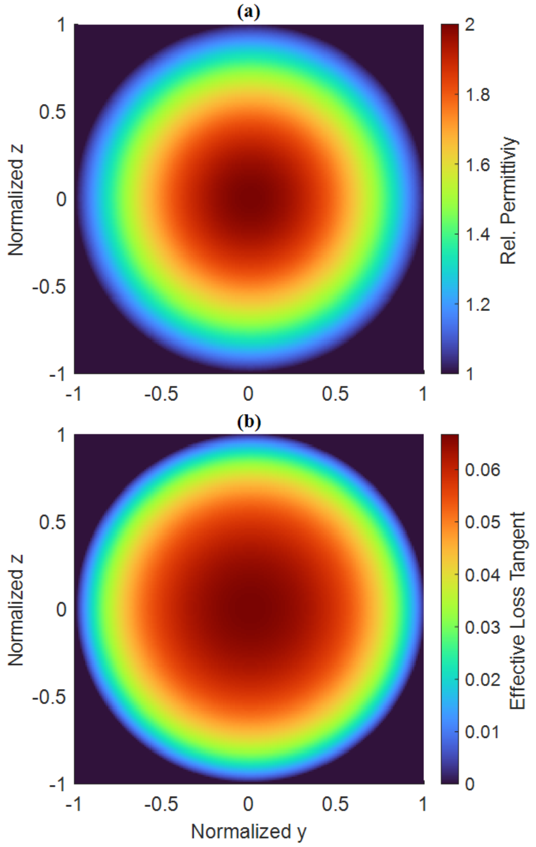

Fig. 2. Relative permittivity in (a) and effective loss tangent in (b) of a LL using Linear mixing rule.

Due to the spherical symmetry of the LL, the choice of the cut plane used in Fig. 2 is arbitrary, and the y-z plane is chosen. Therefore, (5) may be rewritten as:

$$\begin{aligned}\varepsilon_{LB} &= 2 - \left(\frac{y^2+z^2}{r_l^2}\right),\\ &= 2 - \left(\left(\frac{y}{r_l}\right)^2 + \left(\frac{z}{r_l}\right)^2\right),\\ &= 2 - \left((\bar{y})^2 + (\bar{z})^2\right).\end{aligned} \tag{10}$$

For generality, in (10) we have defined the normalized coordinates $\bar{y} = y/r_l$ and $\bar{z} = z/r_l$. By doing so, all points within the lens satisfy $(\bar{y})^2 + (\bar{z})^2 \leq 1$.

Knowing that $\varepsilon'_{Lin} = \varepsilon_{LB}$, (10) is used directly to create Fig. 2 (a). For Fig. 2 (b), the necessary volume fraction for the lens is computed using (9), then the lens complex effective permittivity $\hat{\varepsilon}_{Lin}$ is computed using (7). Since:

$$\hat{\varepsilon}_{Lin} = \varepsilon'_{Lin} - j \cdot \varepsilon''_{Lin}, \tag{11}$$

then by definition, the effective loss tangent is given by:

$$tan\left(\delta_{Lin}\right) = \frac{\varepsilon''_{Lin}}{\varepsilon'_{Lin}}. \tag{12}$$

The Linear rule predicts a greater effective loss tangent for the lens than does the MG rule. This is demonstrated in Fig. 3 for a material with a dielectric constant of 4.0 and a loss tangent of 0.1. For generality, results are plotted with respect to the normalized radius $\bar{r}$, defined as:

$$\bar{r} = \frac{\sqrt{r_c^2 + z^2}}{r_l}. \tag{13}$$

Substitution of $(\bar{r})^2$ into (5) yields:

$$\varepsilon_{LB} = 2 - (\bar{r})^2, \tag{14}$$

noting that for all points within the lens, $0 \leq \bar{r} \leq 1$. Now, since the real part of effective permittivity is required to equal ε_{LB}, then the difference between the two rules must reside in the imaginary component. To show this, the MG prediction is computed by first determining the required volume fraction using (6), and then (3) is applied to compute $\hat{\varepsilon}_{MG}$. The Linear prediction is computed by using (9) to obtain f_{Lin} and then using (7) to compute $\hat{\varepsilon}_{Lin}$. As seen in Fig. 3 (a), $\varepsilon''_{MG} \leq \varepsilon''_{Lin}$, thus $\tan\left(\delta_{MG}\right) \leq \tan\left(\delta_{Lin}\right)$, which is observed in Fig. 3 (b). The disparity widens for materials with larger dielectric constants.

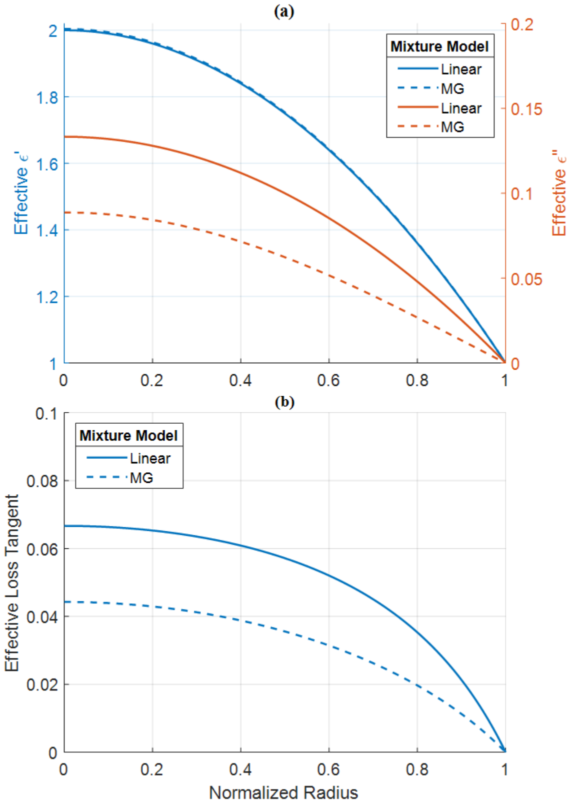

Fig. 3. Comparison of mixture models. In (a), effective ε' and ε'' versus normalized radius. In (b), the effective loss tangent versus normalized radius.

B. Parameter combinations modeled

The AM of a LL requires the use of materials having a dielectric constant of 2 or more. In the simulations conducted for this research, the dielectric constant of the material used to print the lens, takes on one of nine values:

$$\varepsilon' = [2.3, 2.5, 2.8, 3.5, 4, 5, 6, 8, 10]. \tag{15}$$

The non-uniform distribution in (15) has been found necessary to adequately track the gradient of loss for low values of ε'. Figure 4 demonstrates why this is necessary for the specific case of the beam loss factor. The magnitude of the gradient changes quickly for low values of ε'. Therefore, developing an accurate empirical model necessitates denser sampling of ε' in this region. The effect is similar for all loss factors studied in this research. The LL model used to create this figure has a radius of 40λ and a material loss tangent of 0.1.

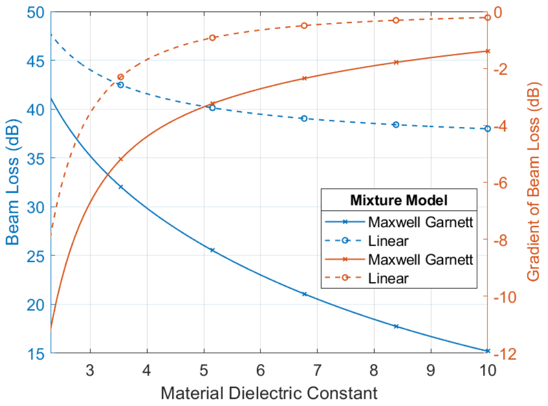

Fig. 4. Maximum beam loss factor and gradient versus material dielectric constant ε'.

For each dielectric constant in (15), a 20 × 20 semi-uniform grid is used to sweep over material loss tangent and lens radius. Thus, loss tangent is swept from 0 to 0.01 in 0.001 increments, and from 0.01 to 0.1 in 0.01 increments. Lens radius is swept from 2 to 40 wavelengths λ, in 2λ increments. A depiction of the sample grid is shown in Fig. 5, using a material with a dielectric constant of 4.0 and MG mixing. Each sample point is the result of a distinct 3D FEA simulation. Moreover, a total of 3,600 FEA simulations are conducted for each of the two mixture models studied. Loss tangents greater than 0.1 are considered too high for practical LL based applications and are therefore not investigated.

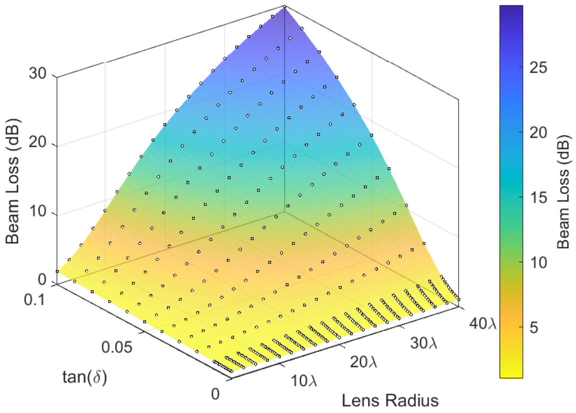

Fig. 5. Sample grid overlaid on surface plot of Beam Loss.

C. Far field loss factors

In this section we describe the specific far field loss factors that are used to quantify and compare antenna performance.

With reference to the spherical coordinate system depicted in Fig. 6, the total radiated power by the antenna, in Watts, is given by [22]:

$$P_r = \frac{P_0}{4\pi}\int_{\phi=0}^{2\pi}\int_{\theta=0}^{\pi} g(\theta,\phi)\sin(\theta)\,d\theta\,d\phi, \tag{16}$$

where $g(\theta,\phi)$ represents the far-field gain and P_0 is the power accepted by the antenna, again in Watts. However, due to the complete symmetry of the model about the z axis, the gain is independent of ϕ. This is observed in Fig. 7 (a), in which $10\cdot\log_{10}(g(\theta,\phi))$ is shown for a LL of radius 2λ. Thus, no loss of information occurs representing the gain as $g(\theta)$. Therefore, (16) reduces to:

$$P_r = \frac{P_0}{2}\int_{\theta=0}^{\pi} g(\theta)\ sin(\theta)\ d\theta. \tag{17}$$

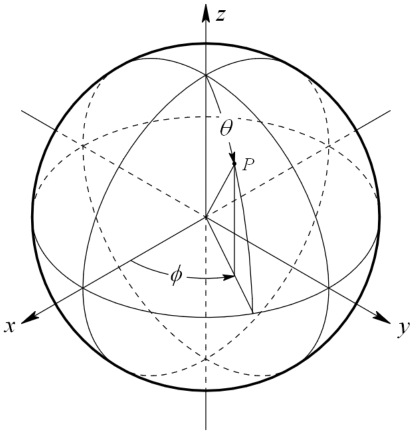

Fig. 6. Spherical coordinate system used to define far-field values, such as antenna gain $g(\theta,\phi)$. The lens is centered at the origin.

We continue by defining P_b as the radiated power contained only in the main beam of the radiation pattern. Defined in Watts, this is given by:

$$\begin{aligned} P_b &= \frac{P_0}{4\pi}\int_{\phi=0}^{2\pi}\int_{\theta=\theta_{FN}}^{\pi} g(\theta,\phi)\sin(\theta)\,d\theta\,d\phi, \\ &= \frac{P_0}{2}\int_{\theta=\theta_{FN}}^{\pi} g(\theta)\ sin(\theta)\ d\theta. \end{aligned} \tag{18}$$

In the above definition, θ_{FN} is the zenith angle corresponding to the first null in the radiation pattern relative to boresight. Upon inspection of the pattern shown in Fig. 7 (b), it is seen that for this example, $\theta_{FN} = 161^\circ \approx 0.894\pi$ radian.

Trapezoidal integration is substituted for the continuous integrals defined in (17) and (18). By estimating θ_{FN} before hand, the angular spacing between pattern samples $\Delta\theta$, is set to ensure accuracy using the numerical

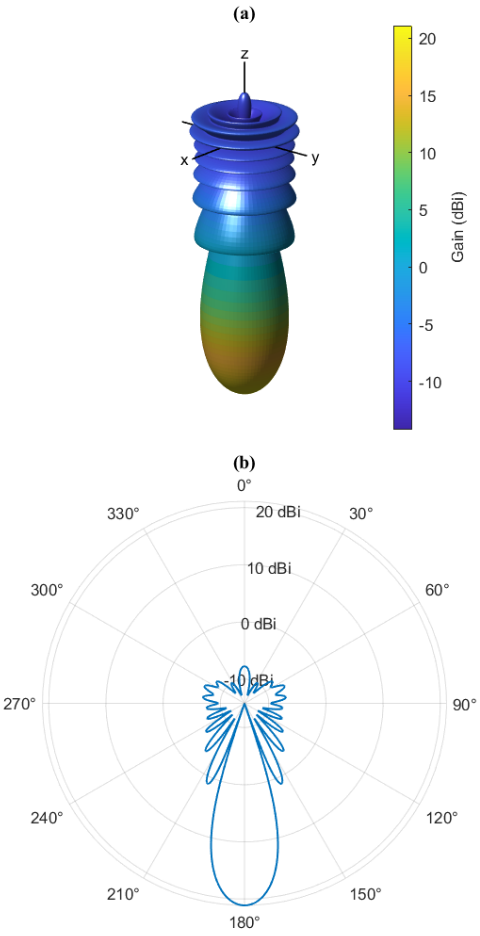

Fig. 7. Example far-field gain pattern. In (a), the full 3D pattern. In (b) a representative 2D cut.

surrogate. After experimentation, a sufficient resolution for this purpose is $\Delta\theta \leq \frac{\theta_{FN}}{20}$. Accurate prediction of θ_{FN} is accomplished using the equation for an ideal Luneburg lens fed by a cosine point source [26]:

$$g_{LB}(\theta) = 4\pi^2 r_l^2 \left[\frac{2\, J_1\left(2\pi\, r_l \sin(\theta)\right)}{2\pi\, r_l \sin(\theta)}\right]^2, \tag{19}$$

where $J_1(\cdot)$ represents the Bessel function of the first kind of order one, and r_l is the lens radius measured in free-space wavelengths λ. Upon application of numerical peak detection on the reciprocal of (19), it is found that to a high degree of accuracy:

$$2 \cdot \theta_{FN} = \frac{70.08^\circ}{r_l}. \tag{20}$$

Now, upon solving for $\Delta\theta$ yields:

$$\begin{aligned}\Delta\theta &\leq \frac{70.08^\circ}{2 \times 20 \times\, r_l}, \\ &\leq \frac{1.75^\circ}{r_l}.\end{aligned} \tag{21}$$

The angle $2 \cdot \theta_{FN}$ is referred to as the First Null Beam Width $FNBW$ [27]:

$$FNBW = 2 \cdot \theta_{FN}. \tag{22}$$

In Fig. 8, a comparison is provided between the $FNBW$ measured using $g(\theta)$ obtained from FEA simulations and with $\tan(\delta) = 0$, to that predicted by (20). For $r_l \geq 10\lambda$, the two match within 0.7°. The minimum $FNBW$ shown is 1.90°, occurring for a lens radius of 40λ. Thus, for large lenses, the FEA matches closely with (20) derived for lens driven by cosine point source.

The radiation efficiency η_r, is defined as [27]:

$$\eta_r = \frac{P_r}{P_0}, \tag{23}$$

and the radiation loss factor is defined as:

$$L_r = -10 \cdot \log_{10}(\eta_r). \tag{24}$$

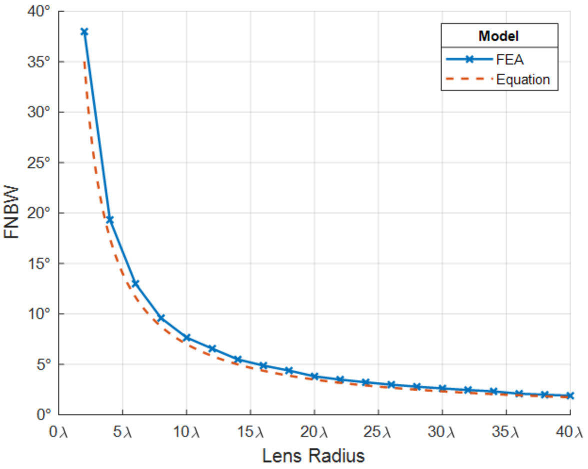

Fig. 8. First Null Beam Width versus lens radius.

The beam efficiency η_b and corresponding loss factor are defined as [27]:

$$\eta_b = \frac{P_b}{P_r}. \tag{25}$$

$$L_b = -10 \cdot \log_{10}(\eta_b). \tag{26}$$

Using (23) and (25), it is obvious that:

$$\frac{P_b}{P_0} = \eta_r \cdot \eta_b, \tag{27}$$

and therefore:

$$L_b + L_r = -10 \cdot \log_{10}\left(\frac{P_b}{P_0}\right). \tag{28}$$

It should be noted that the radiation efficiency only accounts for material losses generated within the LL while the beam efficiency describes the LL's ability to form a beam.

And finally, the aperture efficiency η_a and the corresponding loss factor are defined as [22]:

$$\begin{aligned}\eta_a &= \frac{g(\theta)_{max}}{4\pi^2 r_l^2}, \\ &= \frac{g(\pi)}{4\pi^2 r_l^2}.\end{aligned} \tag{29}$$

$$L_a = 10 \cdot \log_{10}\left(4\pi^2 r_l^2\right) - 10 \cdot \log_{10}\left(g(\pi)\right). \tag{30}$$

In the above, r_l is measured in free-space wavelengths λ. Given the orientation of the waveguide feed, maximum gain occurs at $\theta = 180^\circ = \pi$ rad, which is aligned with the antenna boresight.

D. Curve fitting of loss factors

The loss factors defined in the previous section have an implicit dependence on the mixing rule, the printed material's dielectric constant ε' and loss tangent $\tan(\delta)$, and the lens radius r_l. In this section, new results are presented that show for each loss factor L_x, and each mixing rule y, a rational function curve fit of an auxiliary variable u_y, provides an accurate and wide range empirical model. Thus:

$$L_x^y\left(\varepsilon', \tan(\delta), r_l\right) \approx\, R_x^y(u_y), \tag{31}$$

for $x \in \{a, b, r\}$ and $y \in \{MG, Lin\}$, and where:

$$u_y = \frac{r_l \cdot \tan(\delta)}{F_y(\varepsilon')}. \tag{32}$$

$$R_x^y(u) = \frac{p_1 u^3 + p_2 u^2 + p_3 u + p_4}{u^2 + q_1 u + q_2}. \tag{33}$$

$$F_y(\varepsilon') = \frac{c_1 \cdot (\varepsilon')^{c_2} + c_3}{c_1 \cdot (2.3)^{c_2} + c_3}. \tag{34}$$

The coefficients for (33) are broken into two tables, depending on whether MG or Linear mixing is being modeled. Table 1 contains coefficients for MG mixing and Table 2 for Linear mixing. The coefficients for the pair of normalization functions defined by (34) are provided in Table 3.

Although the procedure used for determining (33) and (34) is heuristic in nature, two distinct steps are

Table 1: R_x^{MG} coefficients. R_{b+r} generates $R_b + R_r$

$\mathbf{R_x}^{\mathbf{MG}}$	$\mathbf{p_1}$	$\mathbf{p_2}$	$\mathbf{p_3}$	$\mathbf{p_4}$	$\mathbf{q_1}$	$\mathbf{q_1}$
R_a	4.02	37.9	77.2	2.31	1.62	2.68
R_b	4.43	25.8	4.19	1.07	0.0793	1.03
R_r	0.309	8.19	5.41	0.003	0.321	0.209
R_{b+r}	4.56	36.3	88.4	2.79	1.38	2.72

Table 2: R_x^{Lin} coefficients. R_{b+r} generates $R_b + R_r$

$\mathbf{R_x}^{\mathbf{Lin}}$	$\mathbf{p_1}$	$\mathbf{p_2}$	$\mathbf{p_3}$	$\mathbf{p_4}$	$\mathbf{q_1}$	$\mathbf{q_1}$
R_a	4.62	42.0	67.3	1.73	1.32	1.98
R_b	4.93	30.9	3.16	0.857	0.115	0.804
R_r	0.283	8.45	3.98	0.0031	0.229	0.133
R_{b+r}	5.25	39.8	80.3	2.19	1.13	2.11

identified. The first step involves experimentation with the MATLAB Curve Fitting Toolbox (CFT) to determine the best functional form of the respective equations. In this regard, the term "best", should be taken as a positive combination of succinctness, flexibility, and accuracy. The choice of the rational function in (33) and the power series in (34), possess these attributes.

With the functional forms of (33) and (34) in hand, the second step involves finding an optimized set of coefficients. For this, the MATLAB Global Optimization Toolbox (GOT) is employed. Whereas the CFT is designed to try out diverse functional fits quickly, it does not search and compare multiple bins of attraction as do the GOT methods [24]. In particular, the GOT provides an efficient implementation of the Multi-Start algorithm and a straightforward optimization framework [28].

Data for the CFT and GOT is comprised of nine three dimensional surfaces as visualized in Fig. 5, for each loss factor and for each mixing rule. The nine surfaces represent the nine dielectric constants of (15) that FEA is conducted. Since each surface contains 400 points, the curve fitters have 3,600 points to work with for each set of coefficients listed in Tables 1-3. Upon completion of the Multi-Start algorithm, the coefficients are saved to appropriately named files for fast access. All results that are reported in this research round the coefficients to three significant digits, as reported in Tables 1-3.

A key observation is that the substitution of u_y in (31), effectively reduces the dimensionality of the problem from three to one. Moreover, since we are now dealing with functions of a single variable, straightforward curve fitting is possible, as in (33). To demonstrate why this is possible, results are presented that first reduce the dimensionality from three to two, and then from two to one.

Table 3: F_{MG} and F_{Lin} coefficients

$\mathbf{F_y}$	$\mathbf{c_1}$	$\mathbf{c_2}$	$\mathbf{c_3}$
F_{MG}	7.57	0.799	-5.13
F_{Lin}	-3.88	-1	3.85

Consider the surface plot of the beam loss factor provided in Fig. 5. This figure is generated using the MG mixture model, with a printed material dielectric constant $\varepsilon' = 4.0$. The loss factor is shown explicitly as a function of the variables r_l and $\tan(\delta)$. However, adapting the notation $L_b^{MG}(\varepsilon', \tan(\delta), r_l)$, we refer to it as a function of three variables, namely: ε', $\tan(\delta)$ and r_l. Alternatively, L_b^{MG} as well as L_b^{Lin}, can be closely approximated as a function of only two variables: ε' and the product $r_l \cdot \tan(\delta)$. This is observed for the FEA results given in Fig. 9 for the MG mixture model and Fig. 10 for Linear mixing. In both figures, results are plotted for the several dielectric constants, i.e., $\varepsilon' = [2.3, 2.8, 4, 10]$, each trace corresponding to a unique ε'.

The resulting traces are not strictly continuous, but nearly so, and especially so for MG mixing and $\varepsilon' \geq 4$. This characteristic is observed for all the loss factors considered in this research. Thus, for a given mixture model, the individual loss factors can be accurately represented as a function of ε' and the product of lens radius r_l times the loss tangent $\tan(\delta)$.

The normalization factors $F_{MG}(\varepsilon')$ and $F_{Lin}(\varepsilon')$ are graphed in Fig. 11. Their purpose is explained below, using an illustrative example. Consider the loss trace in Fig. 9 for $\varepsilon' = 4$, which we will express here as $L_b^{MG}(4, r_l \cdot \tan(\delta))$. Using the coefficients in Table 3 and (34), $F_{MG}(4)$ is found to be ≈ 1.853. Careful

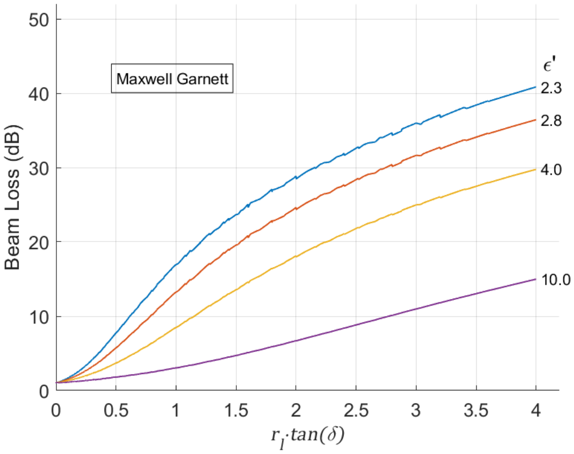

Fig. 9. FEA results showing the beam loss factors versus $r_l \cdot \tan(\delta)$ for the MG mixture model.

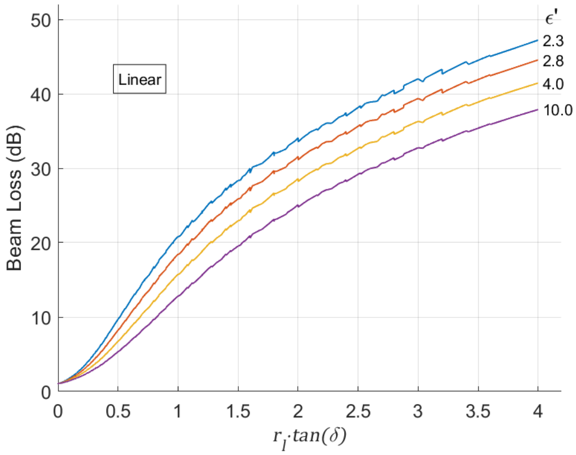

Fig. 10. FEA results showing the beam loss factors versus $r_l \cdot \tan(\delta)$ for the Linear mixture model.

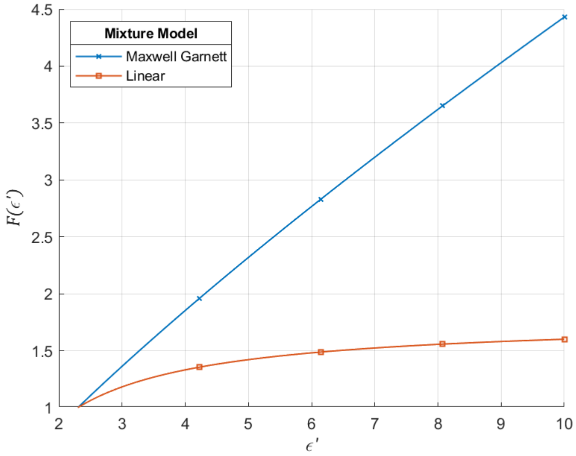

Fig. 11. Normalization factors $F_{MG}(\varepsilon')$ and $F_{Lin}(\varepsilon')$.

examination of Fig. 9 verifies that the following approximation holds:

$$L_b^{MG}(4, r_l \cdot \tan(\delta)) \approx L_b^{MG}\left(2.3, \frac{r_l \cdot \tan(\delta)}{1.853}\right), \quad (35)$$

and in general:

$$L_x^y(\varepsilon\prime, r_l \cdot \tan(\delta)) \approx \, L_x^y\left(2.3, \frac{r_l \cdot \tan(\delta)}{F_y(\varepsilon')}\right). \quad (36)$$

Thus, given an arbitrary ε', the normalization factors map the corresponding loss factors onto respective portions of a reference trace having $\varepsilon' = 2.3$. Since ε' is fixed for the reference trace, we are effectively left with an equation of a single variable u_y, defined by (32). This is demonstrated in Fig. 12, where the FEA results for beam loss are shown for the same set of dielectric constants used in Fig. 9 and Fig. 10. The FEA results for any particular ε', extends from $\left(0, L_b^y(0)\right)$ to the respectively labeled $\circ$ marker. For a given mixture model y, the loss factor can be accurately represented as a function of the single auxiliary variable u_y.

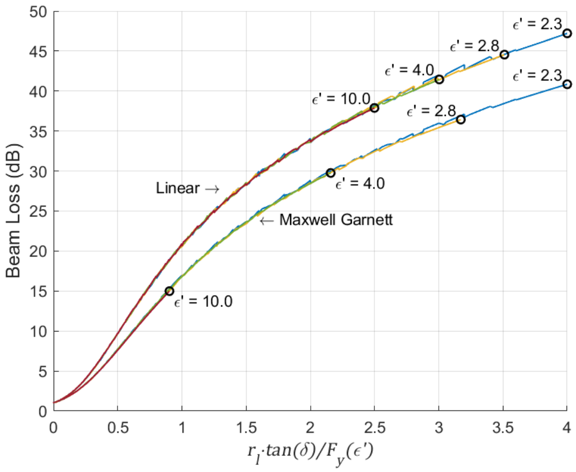

Fig. 12. FEA results showing beam loss factors L_b^{MG} and L_b^{Lin} versus $u_y = r_l \cdot \tan(\delta)/F_y(\varepsilon')$.

Table 4: Study wide rmse of curve fit for loss factors

$\mathbf{R_x}$	$\mathbf{rmse_x^{MG}}$ (dB)	$\mathbf{rmse_x^{Lin}}$ (dB)
R_a	0.074	0.098
R_b	0.073	0.104
R_r	0.027	0.032
R_{b+r}	0.067	0.093

III. RESULTS AND DISCUSSION

In this section the rational function curve fits R_x^y are compared with the respective loss factors L_x^y obtained through FEA simulation. Additionally, R_x^y is used to determine the maximum useful lens radius for several common low loss polymers.

A. Curve fit performance and discussion

Table 4 provides the root mean square error (rmse) of the individual curve fits. On average, the rmse for the Linear mixture fit is 33% higher than that of the MG fit, however, in all cases the errors are below 0.11 dB. The FEA data provided earlier in Fig. 9 and Fig. 10 appears consistent with this result, since the L_b^{Lin} plots do exhibit larger perturbations than their MG counterparts. Note that the function R_{b+r} generates $R_b + R_r$, in which case the respective rmse reported in Table 4 is computed using $(L_b + L_r - R_{b+r})$.

The following contour plots provide further insight to the loss factors observed through FEA, as well as the respective rational function fit. Each figure contains data only for a single dielectric constant, and $\varepsilon' = 2.8$ is chosen as a representative example. Furthermore, plots are shown for the Linear mixture model.

Figure 13 compares the FEA derived beam loss factor L_b^{Lin} with the fit equation R_b^{Lin}. The plot in Fig. 13 (a) is colorized using the L_b^{Lin} data, and constant loss contours of L_b^{Lin} are shown using solid black lines and that of R_b^{Lin} with dashed white lines. Both sets of contours are displayed every 3 dB, with the highest extending to 42 dB. In Fig. 13 (b), the difference between L_b^{Lin} and R_b^{Lin} is shown. Although a peak residual of 0.4 dB is observed, this occurs at $L_b^{Lin} \approx 39$ dB, which should be insignificant for most purposes. The rmse over the plot is 0.107 dB, which is slightly above the rmse reported in Table 4. This is understandable, since Table 4 accounts for all nine values of ε' examined in this research.

Examination of any contour line in Fig. 13 (a) reveals that the product $r_l \cdot \tan(\delta)$ is constant valued along the contour. Since the plot is generated with ε' fixed at 2.8, then $F_{Lin}(\varepsilon')$ is obviously constant, and therefore $r_l \cdot \tan(\delta)/F_{Lin}(\varepsilon')$ must also equate to a constant along the contour. The later expression is defined in (32) as u_{Lin}, and R_b^{Lin} is a rational polynomial in terms of u_{Lin} given by (33). In a sense then, R_b^{Lin} maps the set of points on a given contour line to a scalar which is the loss associated with that contour line. It does so across all values of ε' as well. Moreover, constant loss contour lines are rectangular hyperbolas, but are defined only for positive arguments. This is a common characteristic for all the loss factors addressed in this research, regardless of the mixture model.

Figure 14 (a) compares the FEA derived aperture loss factor L_a^{Lin} with the rational fit R_a^{Lin} and is drawn in the same fashion as Fig. 13 (a). The rmse for this fit is 0.102 dB, just slightly higher than the study wide value reported in Table 4. As with the beam loss factor, the contours are rectangular hyperbolas.

A curve fit for the lens gain in decibels is written directly using the rational function fit for the aperture loss factor as:

$$\check{G}_{Lin} = 10 \cdot \log_{10}\left(4\pi^2 r_l^2\right) - R_a^{Lin}, \qquad (37)$$

and in Fig. 14 (b), it is compared with the FEA derived gain. Even though the gain and aperture loss factor contours are quite different, the rmse of the gain fit is identical to that of aperture loss factor. This must be so, since $\check{G}_{Lin}$ is only dependent upon the lens radius r_l and R_a^{Lin}. Since r_l is known exactly, the error in the gain fit can only originate from R_a^{Lin}.

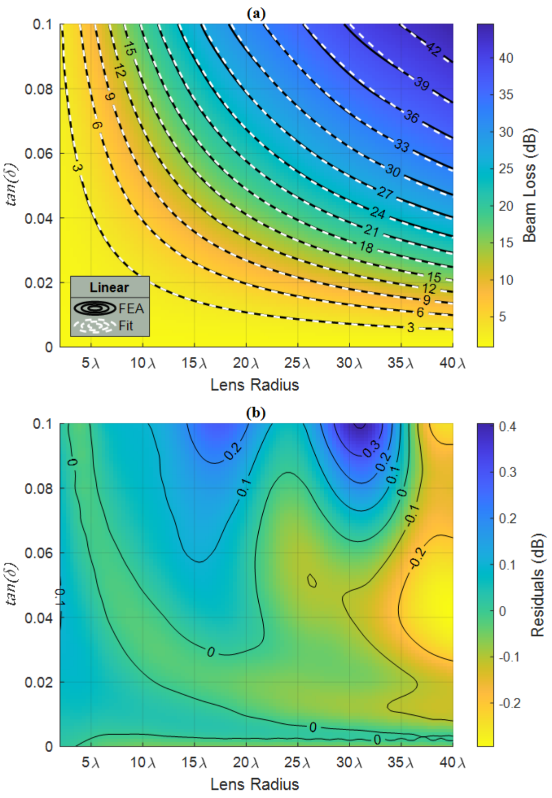

Fig. 13. (a) Illustrates a direct comparison of FEA results L_b^{Lin} and the rational function fit R_b^{Lin} using coefficients from Table 1 and Table 3. (b) Shows the residual difference, $E_b^{Lin} = L_b^{Lin} - R_b^{Lin}$. Printed material $\varepsilon' = 2.8$.

A distinguishing characteristic of the constant gain contours in Fig. 14 (b) is that they have a finite maximum. This implies that for a given ε' and a $\tan(\delta) > 0$, there is a lens radius r_{peak}, at which the gain peaks and increasing r_l beyond r_{peak} can only result in a lower gain. Determination of r_{peak} is attained by solving the derivative of (37) in terms of r_l with the condition that $d\check{G}_{Lin}/dr_l = 0$. In doing so it is found that depending upon the mixture rule being modeled, r_{peak} must lie on either the $R_a^{Lin} \approx 10.14$ dB contour or the $R_a^{MG} \approx 10.39$ dB contour. For example, with $\varepsilon' = 2.8$ and $\tan(\delta) = 0.04$ and linear mixing, then $r_{peak} \approx 8.23\lambda$. Upon reducing the loss tangent to 0.02, yields $r_{peak} \approx 16.5\lambda$. The product $r_{peak} \cdot \tan(\delta)$ is a constant for a given ε' and mixing rule. A red dashed trace in Fig. 14 indicates the respective contour.

Finally, in Fig. 15 is a comparison between the FEA derived radiation loss factor L_r^{Lin} and the fit equation R_r^{Lin}. The rmse for this fit is 0.028 dB, which is slightly below the study wide value provided in Table 4.

It is notable that the maximum radiation loss observed in Fig. 15 (a) is ≈ 9.7 dB, since the maximum beam loss seen in Fig. 13 (a) is ≈ 44.5 dB. For the lossless case, 100% of the power accepted by the lens is radiated, and between 78% to 80% of the radiated power is contained within the main lobe. As loss is introduced, the radiated power naturally decreases. For instance, along the 9 dB loss contour shown in Fig. 15 (a), only 13% of the accepted power is being radiated. Furthermore, the same combinations of r_l and $\tan(\delta)$ that produce a 9 dB radiation loss, produce ≈ 14.8 dB beam loss in

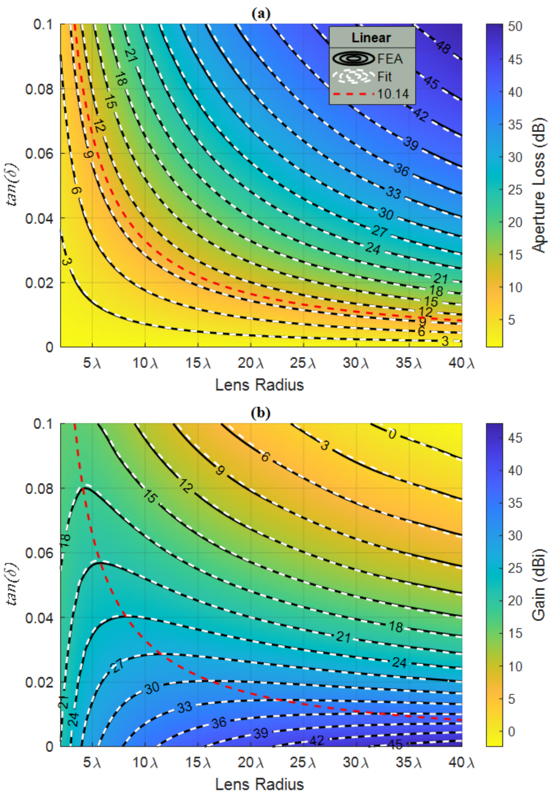

Fig. 14. (a) Illustrates a direct comparison of FEA results L_a^{Lin} and R_a^{Lin}. (b) Illustrates a direct comparison of FEA derived gain and the fit provided by $\check{G}_{Lin}$. Red trace is hyperbola marking locus of gain peaks. $\varepsilon' = 2.8$.

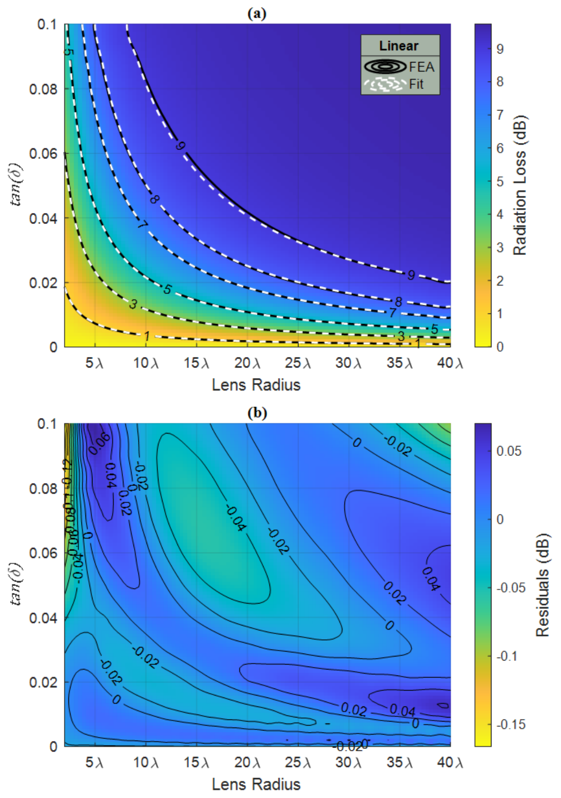

Fig. 15. (a) Illustrates a direct comparison of FEA results L_r^{Lin} and the rational function fit R_r^{Lin}. (b) Shows the residual difference, $E_r^{Lin} = L_r^{Lin} - R_r^{Lin}$. $\varepsilon' = 2.8$.

Fig. 13 (a). This means that ≈ 3% of the radiated power is now contained in the main beam. At the severest point simulated, that being the top right corner of the contour plots, the radiation loss has only increased by another 0.7 dB, and therefore the radiated power is very nearly the same being ≈ 11% of accepted. However, the beam loss has increased by 29.7 dB, therefore reducing the power in the main beam to approximately 0.0035% of the radiated power.

B. Maximum useful lens radius of common polymers

We have shown that for each loss factor L_x, and each mixing rule y, a rational function curve fit of an auxiliary variable $u_y = r_l \cdot \tan(\delta)/F_y(\varepsilon')$, provides an accurate and wide range empirical model of that loss factor. We now further define the normalized loss tangent as being:

$$t_y = \frac{tan(\delta)}{F_y(\varepsilon')}, \tag{38}$$

thus:

$$u_y = r_l \cdot t_y, \tag{39}$$

and therefore:

$$L_x^y \approx R_x^y(r_l \cdot t_y). \tag{40}$$

The purpose of (38) is more than convenience and will be evident shortly. Up to now, we have been utilizing contour plots that visualize loss and gain by treating ε' as a constant and r_l and $\tan(\delta)$ as independent variables. This provides the most direct method to compare FEA results to the rational function approximations. As a comparative design aide though, it is cumbersome since a separate plot is needed for every ε' being considered. Therefore, we now treat r_l and t_y as independent variables. Since t_y encapsulates the loss characteristics of a particular lens material, a single contour plot facilitates visualization of loss as r_l is varied across an infinite set of materials.

This is done in Fig. 16 for the rational function approximation of the input referred beam loss factor $L_b^{MG} + L_r^{MG} = -10 \cdot \log_{10}(P_b/P_0)$. This is an important performance metric, since P_b/P_0 is the ratio of power radiated in the main beam to the power accepted by the lens. Logarithmic scales are used for both r_l and t_{MG} due to the relatively large range of values. The diagonal traces are constant $L_b^{MG} + L_r^{MG}$ contours and are remarkably linear. The vertical red dashed lines show the locus of points that represent $L_b^{MG} + L_r^{MG}$ associated with the

Table 5: Polymers considered in this research

ID	Material
A	High Density Polyethylene [19]
B	Low Density Polyethylene [19]
C	Polytetrafluoroethylene (PTFE) [19]
D	Polypropylene (PP) [20]
E	Polycarbonate (PC) [15]
F	Acrylonitrile butadiene styrene (ABS) [15]
G	DSM Somos NanoTool [15]
H	DSM Somos ProtoGen 18120 [16]
I	DSM Somos ProtoTherm 12120 [15]
J	DSM Somos Watershed 11122 [15]

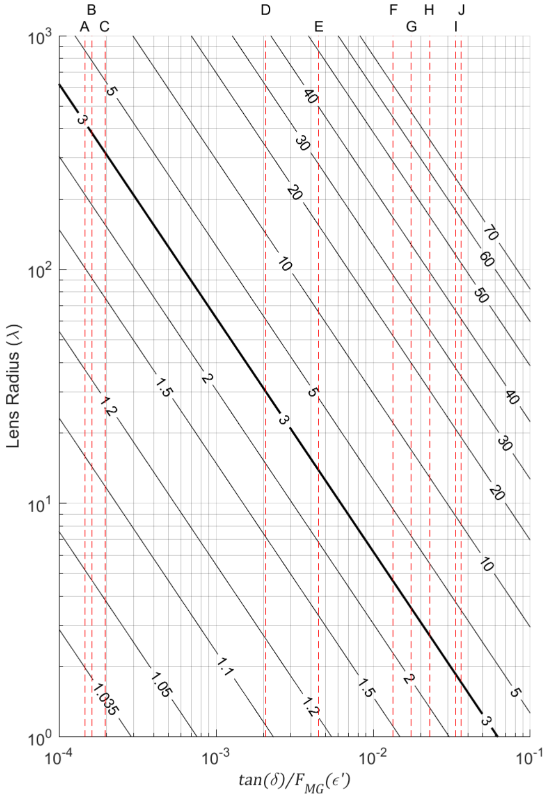

Fig. 16. Beam loss relative to P_0 as lens radius r_l and the normalized loss tangent t_{MG} are varied. Contour labels are in dB.

constant t_{MG} for the material identified by the capital letter directly above the trace. These traces are labeled A through I and refer to the polymers listed in Table 5. In Table 6, the published dielectric constant and loss tangent of each polymer is listed, along with the respective normalization factor and normalized loss tangent computed for MG mixing.

Table 6: Polymer properties along with normalization factor and normalized loss tangent for MG mixing

ID	ε'	$\tan(\delta)$	$\mathbf{F_{MG}}(\varepsilon')$	$\mathbf{t_{MG}}$
A	2.35	1.5×10^{-4}	1.03	1.46×10^{-4}
B	2.28	1.6×10^{-4}	0.989	1.62×10^{-4}
C	2.05	1.70×10^{-4}	0.865	1.96×10^{-4}
D	2.23	2.00×10^{-3}	0.963	2.08×10^{-3}
E	2.59	5.20×10^{-3}	1.15	4.51×10^{-3}
F	2.54	1.51×10^{-2}	1.13	1.34×10^{-2}
G	3.2	2.55×10^{-2}	1.46	1.74×10^{-2}
H	3.16	3.30×10^{-2}	1.44	2.29×10^{-2}
I	2.88	4.37×10^{-2}	1.30	3.36×10^{-2}
J	2.62	4.24×10^{-2}	1.17	3.63×10^{-2}

The 3 dB contour in Fig. 16 is of particular interest since it identifies the combinations of material and lens radius that produce a radiation pattern in which half of the accepted power is contained in the main lobe, with the remaining half lost to heating and side lobes. Points to the right of the 3 dB contour have greater main lobe loss, and points to the left have less. Thus, for any point on the contour, increasing either r_l, t_{MG} or both, results in a main lobe containing less than half of the accepted power. We solve for the intersection of each red trace with the 3 dB contour, and consider the associated r_l as the maximum useful lens radius for the respective material. The same procedure is repeated using the Linear mixing rule. Compared to MG mixing, the Linear rule always produces a smaller useful radius, i.e., it produces greater loss. Thus, the Linear mixture provides a lower bound and the MG mixture an upper. Taken together, the Linear and MG predictions are considered as a range of useful radii, with the actual value dependent upon the mixing model employed. This data is reported in the second column of Table 7. An interesting occurrence is that regardless of mixing rule or the material, L_b and L_r are fixed values along any constant $L_b + L_r$ contour. For the 3 dB contour, $L_b = 1.41$ dB and $L_r = 1.59$ dB.

A similar contour plot of the the rational function approximation of lens gain $G = 10\cdot\log_{10}\left(4\pi^2 r_l^2\right) - L_a^{MG}$ is provided in Fig. 17. Additionally, the 3 dB contour from Fig. 16 is superimposed. We solve for the gain at the intersection of each red line with the overlaid $L_b^{MG} + L_r^{MG}$ contour and consider this the maximum useful gain of the lens. This is also carried out for Linear mixing, which always results in lower gain. The two values are considered as the range that may occur depending upon the mixing model, and are reported in the third column of Table 7.

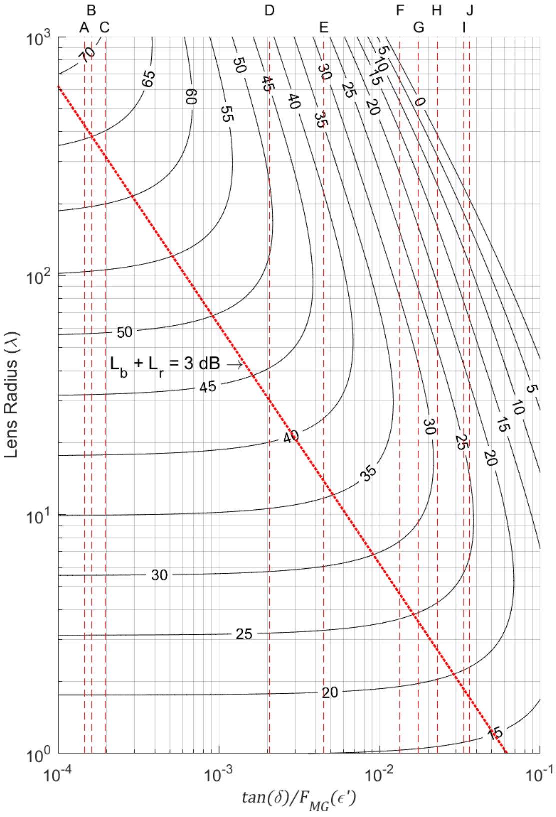

Fig. 17. Antenna gain as lens radius r_l and the normalized loss tangent t_{MG} are varied. Contour labels are in dB.

Table 7: Maximum useful lens radius and gain (Lin : MG)

ID	$\mathbf{r_{max}}\,(\lambda)$	$\mathbf{G_{max}}$ **(dBi)**
A	356 : 425	64.4 : 65.9
B	326 : 384	63.6 : 65.1
C	279 : 316	62.3 : 63.4
D	25.6 : 29.9	41.5 : 42.9
E	11.0 : 13.8	34.2 : 36.1
F	3.73 : 4.64	24.8 : 26.7
G	2.51 : 3.57	21.3 : 24.4
H	1.93 : 2.72	19.0 : 22.1
I	1.39 : 1.85	16.2 : 18.7
J	1.36 : 1.71	16.0 : 18.0

C. The product $\mathbf{r_l \cdot t_y}$

The product of the lens radius r_l in terms of λ and the normalized loss tangent t_y is a key metric in characterizing the radiation pattern of a LL with loss. This is because $L_x^y \approx R_x^y(r_l \cdot t_y)$ as pointed out in the previous section. The product $r_l \cdot t_y$ therefore provides a succinct method to specify thresholds of operation for the LL with loss. This is done in Table 8 for the three thresholds that have been discussed earlier in Sections III-A and III-B.

Table 8: Thresholds of performance and associated $r_l \cdot t_y$ products

Threshold Description	$\mathbf{r_l \cdot t_{Lin}}$	$\mathbf{r_l \cdot t_{MG}}$
50% of accepted power is contained within the main beam, i.e., $\eta_r \eta_b = 0.5$. **Note**: $L_b = 1.41$, $L_r = 1.59$ dB regardless of mixture.	0.0525	0.0622
Gain at peak value for given material and mixture. Increasing r_l can only decrease the gain. **Note**: The aperture loss differs slightly with mixture: $L_a^{Lin} = 10.14$, $L_a^{MG} = 10.39$ dB.	0.289	0.360
13% of accepted power is radiated, and ≈ 3% of the radiated power is contained in the main beam. **Note**: The beam efficiency differs slightly with mixture: $\eta_b^{Lin} = 0.033$, $\eta_b^{MG} = 0.028$. Note that 13% accepted equates to an $L_r = 9$ dB.	0.715	0.922

IV. CONCLUSION

This research has applied EMT and 3D FEA to model the transmissive loss through a waveguide fed additively manufactured Luneburg lens. It is found that rational function approximations accurately model antenna loss factors derived from this modeling. Using this empirical model of loss, the following conclusions are drawn.

For a given mixing rule y, it is the product of lens radius r_l and the polymers normalized loss tangent t_y, that ultimately determine the transmissive loss of the lens. The normalized loss tangent is itself, a function of the polymer's dielectric constant ε' and its loss tangent $\tan(\delta)$. When comparing the relative merits of two different polymers, neither ε' nor $\tan(\delta)$ taken alone are sufficient to make the best choice. However, choosing the material with the lowest t_y, is guaranteed to result in the lowest transmissive loss.

Given that transmissive loss is dependent on the product $r_l \cdot t_y$, a maximum r_l exists for each combination of mixing rule, polymer and level of loss that is deemed tolerable. In this research, the threshold of useful operation occurs when half of the accepted power by the antenna is radiated in the main lobe. Therefore, for a given mixing rule, once the polymer is chosen, the engineer can determine the maximum useful lens radius. In turn, this determines maximum gain achievable G_{max}, which is the value of G when the main lobe contains exactly 50% of the accepted power.

The product $r_l \cdot \ t_y$ provides a concise method to specify thresholds of operation for the LL with loss. It is of course dependent upon the mixing rule, but even so, immediately indicates important aspects of the radiation pattern and thus the performance. Three thresholds have been identified and tabulated. Regardless of mixture rule, values below 0.05 result in greater than 50% of the accepted power being radiated in the main beam. Thus, this simple rule can guide material selection. Other factors being equal, the Linear mixing rule always produces greater loss than the MG rule. Taken together, the two EMT rules set lower and upper bounds of performance. Examining Table 7, it is observed that the difference in G_{max} predicted by these two theories ranges between 1.4 dB and 3.1 dB for practical size lenses. At present however, the unit cell structures used in AM graded index components do not seem to obey the MG mixing law [5]. Rather, they more closely follow the Bruggeman and Capacitive model, which are both better approximated by the Linear mixing rule [25]. To maximize gain, research into producing unit cell arrangements that follow the MG mixing law is therefore still needed.

REFERENCES

[1] R. K. Luneburg, *Mathematical Theory of Optics*. Brown University Press, Providence, RI, USA, 1944.

[2] P. S. Hall and S. J. Vetterlein, “Review of radio frequency beamforming techniques for scanned and multiple beam antennas,” *IEEE Proc. Microwaves, Antennas Propag.*, vol. 137, no. 5, pp. 293-303, 1990.

[3] Y. Li, Lei G. M. Chen, Z. Zhang, Z. Li, and J. Wang, “Multibeam 3-D-printed Luneburg lens fed by magnetoelectric dipole antennas for millimeter-wave MIMO applications,” *IEEE Trans. Antennas Propag.*, vol. 67, no. 5, pp. 2923-2933, May 2019.

[4] J. Deroba, A. Good, K. Sobczak, Z. Larimore, and M. S. Mirotznik, “Additively manufactured Luneburg retroreflector,” *IEEE Trans. Aerospace Electronic Syst.*, Sep. 2019.

[5] M. Liang, W.-R. Ng, K. Chang, K. Gbele, M. E. Gehm, and H. Xin, “A 3-D Luneburg lens antenna fabricated by polymer jetting rapid prototyping,” *IEEE Trans. Antennas Propag.*, vol. 62, no. 4, pp. 1799-1807, 2014.

[6] Z. Larimore, S. Jensen, P. Parsons, B. Good, K. Smith, and M. S. Mirotznik, “Use of space-filling curves for additive manufacturing of three dimensionally varying graded dielectric structures using fused deposition modeling,” *Additive Manuf.*, vol. 15, pp. 48-56, 2017.

[7] Z. Larimore, S. Jensen, A. Good, J. Suarez, and M. S. Mirotznik, “Additive manufacturing of Luneburg lens antennas using space-filling curves and fused filament fabrication,” *IEEE Trans. Antennas Propag.*, vol. 66, no. 6, pp. 2818-2827, 2018.

[8] S. Biswas, A. Lu, Z. Larimore, P. Parsons, A. Good, N. Hudak, B. Garrett, J. Suarez, and M. S. Mirotznik, “Realization of modified Luneburg lens antenna using quasi-conformal transformation optics and additive manufacturing,” *Microwave Optical Technol. Lett.*, vol. 61, no. 4, pp. 1022-1029, 2019.

[9] S. Biswas and M. S. Mirotznik, “High gain, wide-angle QCTO-enabled modified Luneburg lens antenna with broadband anti-reflective layer,” *Nature: Sci. Rep.*, vol. 10, no. 1, pp. 1-13, 2020.

[10] O. Bjorkqvist, O. Zetterstron, and O. Quevedo-Teruel, “Additive manufactured dielectric Gutman lens,” *Electronic Lett.*, vol. 55, no. 25, pp. 1318-1320, 2019.

[11] J. Poyanco, F. Pizarro, and E. Rajo-Iglesias, “3D-printing for transformation optics in electromagnetic high-frequency lens applications,” *Materials*, vol. 13, pp. 1-11, 2020.

[12] P. Liu, X. Zhu, Y. Zhang, J. Li, and Z. Jiang, “3D-printed cylindrical Luneburg lens antenna for millimeter wave applications,” *Int. J. RF Microwave Comput.-Aided Eng.*, vol. 30, pp. 1-8, 2019.

[13] C. Wang, J. Wu, and Y. Guo, “A 3-D printed multibeam dual circularly polarized Luneburg lens antenna based on quasi-icosahedron models for Ka-band wireless applications,” *IEEE Trans. Antennas Propag.*, vol. 68, no. 8, pp. 5807-5815, 2020.

[14] K. Hoel, S. Kristoffersen, M. Ignatenko, and D. Filipovic, “Half ellipsoid Luneburg GRIN dielectric lens loaded double ridged horn antenna,” in *Proc. IET 12th Eur. Conf. Antennas Propag.*, London, UK, 2018.

[15] P. I. Deffenbaugh, R. C. Rumpf, and K. H. Church, “Broadband microwave frequency characterization of 3-D printed materials,” *IEEE Trans. Compon. Packaging Manuf. Technol.*, vol. 3, no. 12, pp. 2147-2155, 2013.

[16] J. Monkevich and G. Le Sage, “Design and fabrication of a custom-dielectric Fresnel multi-zone plate lens antenna using additive manufacturing techniques,” *IEEE Access*, vol. 7, 2019.

[17] J. Zechmeister and J. Lacik, "Complex relative permittivity measurement of selected 3D-printed materials up to 10 GHz," in *Proc. IEEE Conf. Microwave Techn.*, Pardubice, Czech Republic, 2019.

[18] Y. Li and Q. Zhu, "Luneburg lens with extended flat focal surface for electronic scan applications," *Optics Express*, vol. 24, no. 7, 2016.

[19] J. Krupka, "Measurements of the complex permittivity of low loss polymers at frequency range from 5 GHz to 50 GHz," *IEEE Microwave Wireless Compon. Lett.*, vol. 26, no. 6, pp. 464-466, 2016.

[20] J. K, Pakkathillam, B. T. Sivaprakasam, J. Poojali, C. V. Krishnamurthy, and K. Arunachalam, "Tailoring antenna focal plane characteristics for a compact free-space microwave complex dielectric permittivity measurement setup," *IEEE Trans. Instrum. Meas.*, vol. 70, 2021.

[21] A. Sihvola, *Electromagnetic Mixing Formulas and Applications*. London, U.K.: The Institution of Engineering and Technology, 2008.

[22] R. C. Johnson, *Antenna Engineering Handbook*. McGraw-Hill, New York, NY, USA, 1993.

[23] COMSOL Multiphysics§v. 5.6. Stockholm, Sweden: COMSOL AB. Available: www.comsol.com.

[24] MATLAB, ver. 2021a. Natick, MA, USA: The Mathworks Inc., 2021.

[25] E. Burden, Y. Oh, B. Mummareddy, D. Negro, P. Cortes, A. Du Plessis, E. MacDonald, J. Adams, F. Li, and R. Rojas, "Unit cell estimation of volumetrically-varying permittivity in additively manufactured ceramic lattices with X-ray computed tomography," *Mater. Des.*, vol. 210, Nov. 15, 2021.

[26] G. Guo, Y. Xia, C. Wang, M. Nasir, and Q. Zhu, "Optimal radiation pattern of feed of Luneburg lens for high-gain application," *IEEE Trans. Antennas Propag.*, vol. 68, no. 12, pp. 8139-8143, Dec. 2020.

[27] C. A. Balanis, *Antenna Theory - Analysis and Design*. Hoboken, NJ, USA: John Wiley & Sons Inc., 2005.

[28] M. Dourado, J. Meireles, and A. Rocha, "A global optimization approach applied to structural dynamic updating," in *Proc. 14th Int. Conf. Comput. Sci. Its Appl. (ICCSA)*, vol. 8580, pp. 195-210, 2014.

Brian F. LaRocca received the B.S.E.E and M.S.E.E degrees from New Jersey Institute of Technology, Newark, NJ, USA in 1985 and 2000 respectively. From 1985 to 1996 he worked in industry, 1996 to 2004 as a government contractor, and 2004 to present as a civilian engineer with the Dept. of the Army at Ft. Monmouth, NJ, USA and Aberdeen Proving Ground, MD, USA. He received the Ph.D. degree in electrical engineering from the University of Delaware, Newark, DE, USA in the summer of 2022.

Mark S. Mirotznik (S'87–M'92–SM'11) received the B.S.E.E. degree from Bradley University, Peoria, IL, USA, in 1988, and the M.S.E.E. and the Ph.D. degrees from the University of Pennsylvania, Philadelphia, PA, USA, in 1991 and 1992, respectively. From 1992 to 2009, he was a Faculty Member with the Department of Electrical Engineering, The Catholic University of America, Washington, DC, USA. Since 2009, he has been a Professor and an Associate Chair for Undergraduate Programs with the Department of Electrical and Computer Engineering, University of Delaware, Newark, DE, USA. He holds the position of Senior Research Engineer with the Naval Surface Warfare Center, Carderock Division. His current research interests include applied electromagnetics and photonics, computational electromagnetics, multifunctional engineered materials, and additive manufacturing.